

Warming the early Earth - CO₂ reconsidered

Philip von Paris^{a,*}, Heike Rauer^{a,b}, J. Lee Grenfell^{a,b},
Beate Patzer^b, Pascal Hedelt^a, Barbara Stracke^a,
Thomas Trautmann^c and Franz Schreier^c

^a*Institut für Planetenforschung, Deutsches Zentrum für Luft- und Raumfahrt,
Rutherfordstr. 2, 12489 Berlin (Germany)*

^b*Zentrum für Astronomie & Astrophysik, Technische Universität Berlin,
Hardenbergstr. 36, 10623 Berlin, (Germany)*

^c*Institut für Methodik der Fernerkundung, Deutsches Zentrum für Luft- und
Raumfahrt, Münchener Str. 20, 82234 Wessling (Germany)*

Abstract

Despite a fainter Sun, the surface of the early Earth was mostly ice-free. Proposed solutions to this so-called "faint young Sun problem" have usually involved higher amounts of greenhouse gases than present in the modern-day atmosphere. However, geological evidence seemed to indicate that the atmospheric CO₂ concentrations during the Archaean and Proterozoic were far too low to keep the surface from freezing. With a radiative-convective model including new, updated thermal absorption coefficients, we found that the amount of CO₂ necessary to obtain 273 K at the surface is reduced up to an order of magnitude compared to previous studies. For the late Archaean and early Proterozoic period of the Earth, we calculate that CO₂ partial pressures of only about 2.9 mb are required to keep its surface from freezing which is compatible with the amount inferred from sediment studies. This conclusion was not significantly changed when we varied model parameters such as relative humidity or surface albedo, obtaining CO₂ partial pressures for the late Archaean between 1.5 and 5.5 mb. Thus, the contradiction between sediment data

and model results disappears for the late Archaean and early Proterozoic.

Key words:

Faint Young Sun problem, Earth - Atmospheres, composition - Radiative transfer

1 Introduction

2 Geological evidence has shown that liquid water was present on the Earth's sur-
3 face earlier than 3.7 Gy ago (e.g., Mojzsis et al., 1996; Rosing and Frei, 2004)
4 which implies average temperatures on the surface above 273 K. Some authors
5 have even argued for a hot Archaean climate ($T > 340$ K), based on oxygen
6 (Knauth and Lowe, 2003) and silicon (Robert and Chaussidon, 2006) isotope
7 analysis of seawater cherts. However, as pointed out by, e.g., Kasting and Howard
8 (2006) and Shields and Kasting (2007), these isotopic signatures changes might
9 not only be caused by temperature effects. Sleep and Hessler (2006), for ex-
10 ample, deduced a more moderate surface temperature below 300 K, based on
11 quartz weathering records in paleosols. Nevertheless, it is generally accepted
12 that the Earth has been ice-free throughout most of its history.

13 Observations of several solar-type stars of different ages and virtually all stan-
14 dard models of the solar interior have shown that the total solar luminosity has
15 increased since the ZAMS (Zero Age Main Sequence) by about 30% (Gough,
16 1981; Caldeira and Kasting, 1992). Had the composition of the Earth's atmo-
17 sphere been the same then as today, the reduced solar flux would have resulted
18 in surface temperatures below 273 K prior to 2.0 Gy (Sagan and Mullen, 1972).
19 This apparent contradiction between solar evolution models, climatic simula-
20 tions and geological evidence for liquid water and moderately warm tempera-
21 tures on Earth has been termed the "faint young Sun problem".

22 Numerous studies have attempted to solve this problem. For example, Minton and Malhotra

* Corresponding author: philip.vonparis@dlr.de

23 (2007) explored the hot early Sun scenario for a non-standard solar evolution.
24 Shaviv (2003) showed that moderate greenhouse warming in combination with
25 the influence of solar wind and cosmic rays on climate could resolve the prob-
26 lem. Jenkins (2000) assumed high obliquities in a General Circulation Model
27 to account for high Archaean temperatures.

28 However, the most accepted scenario involves a much enhanced greenhouse
29 effect (GHE) on the early Earth compared to modern Earth. Today, the GHE
30 produces around 30 K of warming, raising the mean surface temperature of the
31 Earth to about 288 K. Increased abundances of greenhouse gases such as car-
32 bon dioxide (Kasting, 1987), methane (Pavlov et al., 2000), ethane (Haqq-Misra et al.,
33 2008) or ammonia (Sagan and Mullen, 1972; Sagan and Chyba, 1997) will strengthen
34 the GHE, hence potentially resolve the problem. However, all of these studies
35 faced some form of contradictions or large uncertainties, either from geological
36 data on atmospheric conditions or from atmospheric modeling. The formation
37 and destruction of ammonia is highly dependent on UV levels in the atmo-
38 sphere (Sagan and Chyba, 1997; Pavlov et al., 2001). The hydrocarbon haze
39 necessary to allow higher hydrocarbons to accumulate in the atmosphere de-
40 pends critically on the CO_2/CH_4 ratio (Pavlov et al., 2003). The high values
41 of methane required to heat the surface of the early Earth depend on estimates
42 of the early biosphere and volcanic activity, which is not well determined. Past
43 CO_2 concentrations required by atmospheric models (Kasting, 1987) to reach
44 surface temperatures above 273 K are in conflict with inferred concentrations
45 from the sediment data (Hessler et al., 2004; Rye et al., 1995).

46 In this work, the role of CO_2 in warming the early Earth is reconsidered. We
47 used a one-dimensional radiative-convective model, including updated absorp-
48 tion coefficients in its radiation scheme for thermal radiation. The model was
49 applied to the atmosphere of the early Earth in order to investigate the effect
50 of enhanced carbon dioxide on its climate. Additionally, we investigated the
51 effect of two important parameters, namely the surface albedo and the relative

52 humidity, upon the resulting surface temperature.

53 Our results imply that the amount of CO₂ needed to warm the surface of early
54 Earth might have been over-estimated by previous studies. Furthermore, the
55 results show that the contradiction between modelled CO₂ concentrations and
56 measured values might disappear by the end of the Archaean.

57 Section 2 describes the model and section 3 the runs to validate the new radia-
58 tion scheme. The runs performed for this work are explained and summarized
59 in section 4. In section 5, the results are presented and discussed. Section 6
60 gives the summary of the results.

61 **2 Atmospheric Model**

62 We used a one-dimensional radiative-convective model based on the climate
63 part of the model used by Segura et al. (2003) and Grenfell et al. (2007a,b).
64 Our model differs in upgrades of the radiation scheme to calculate the thermal
65 emission in the atmosphere. The model calculates globally, diurnally-averaged
66 atmospheric temperature and water profiles for cloud-free conditions. We will
67 first state some basic characteristics of the model (2.1). Then we will describe
68 the calculation of the energy transport via radiative transfer (solar and thermal
69 fluxes) and convection (2.2) to obtain the atmospheric temperature profile.
70 Thereafter, a description of the determination of the water profile is given
71 (2.3). Finally, the model input parameters are summarized (2.4).

72 *2.1 Basic model description*

73 The model determines the temperature profile by assuming two dominant
74 mechanisms of energy transport, i.e. radiative transfer and convection. The
75 convective lapse rate is assumed to be adiabatic. The radiative lapse rate is

76 calculated from contributions of both solar and thermal radiation, including
77 Rayleigh scattering for solar radiation and continuum absorption in the ther-
78 mal region. Table 1 summarizes the contributions of the different atmospheric
79 species to the calculation of the temperature profile.

80 The species considered in the model are molecular nitrogen, water, molecular
81 oxygen, argon, carbon dioxide and carbon monoxide. For example, a typi-
82 cal early Earth run considered 0.77 bar of nitrogen and several (2.9 - 57.2)
83 mb of carbon dioxide in addition to water in varying concentrations (0.5—1
84 % at the surface). Molecular nitrogen is an effective Rayleigh scatterer (al-
85 though not as effective as carbon dioxide) and as a main constituent of the
86 atmosphere also contributes to the heat capacity. Water is not considered to
87 be an important Rayleigh scatterer, but it is relevant for the other radiative
88 processes. Also, water influences the adiabatic lapse rate because it readily
89 condenses in the troposphere. However, due to small mixing ratios, especially
90 in the stratosphere, water vapour does not contribute to the heat capacity of
91 the atmosphere. Molecular oxygen and argon do contribute to the heat capac-
92 ity of the atmosphere, and molecular oxygen additionally contributes to the
93 Rayleigh scattering coefficient. Carbon dioxide contributes to all relevant ra-
94 diative mechanisms (molecular absorption of solar and thermal radiation, con-
95 tinuum absorption, Rayleigh scattering), but not to the adiabatic lapse rate
96 because it does not condense under conditions described in this paper. Carbon
97 monoxide is an important absorber species in some mid-infrared windows and
98 contributes to the heat capacity.

99 The model assumes the hydrostatic relation between pressure p and density
100 ρ throughout the plane-parallel atmosphere. On the 52 model layers, a loga-
101 rithmic pressure grid is calculated. Specified pressure levels at the planetary
102 surface (e.g., 1 bar for the standard Earth case) and the upper model lid (at
103 $6.6 \cdot 10^{-5}$ bar) determine the altitude range which, for modern Earth conditions,
104 extends to 65-70 km, i.e. the lower- to mid mesosphere. For all gases except

105 water, the ideal gas law is taken as the equation of state (see 2.2.4 for water).
 106 The effect of clouds is difficult to incorporate into 1D models (see, for example,
 107 Pavlov et al., 2000; Segura et al., 2003). In the present model, following the
 108 approach of Segura et al. (2003), clouds are implicitly included by adjusting
 109 the surface albedo A_{surf} such that under modern Earth control conditions the
 110 model calculates a mean surface temperature of 288 K. The required value for
 111 A_{surf} is about 0.21, whereas the actual global value for Earth is approximately
 112 0.15. This can be interpreted as a ground cloud layer instead of tropospheric or
 113 stratospheric clouds. The model uses a time-stepping algorithm to convergence
 114 to the steady-state solution (Pavlov et al., 2000).

115 2.2 Temperature profile

116 During each time step, the temperature profile is calculated from the radiative
 117 equilibrium condition. The temperature T on an atmospheric level z is
 118 determined by the following equation of energy conservation (Pavlov et al.,
 119 2000):

$$\frac{d}{dt}T(z) = -\frac{g}{c_p(T, z)} \frac{dF(z)}{dp(z)} \quad (1)$$

120 where dt is the time step in the model, c_p the heat capacity, F the total net
 121 radiative flux and p the pressure of the level. The radiative flux F is the sum of
 122 thermal planetary and atmospheric emission, F_{thermal} , and the solar radiative
 123 input, F_{solar} , into the atmosphere:

$$F(z) = F_{\text{thermal}}(z) + F_{\text{solar}}(z) \quad (2)$$

124 These fluxes are calculated separately by two numerical schemes which solve
 125 the monochromatic radiative transfer equation (RTE) for the spectral intensity
 126 I_ν in the respective spectral domain (i.e., near-UV to near-IR for solar flux,

127 near-IR to far-IR for thermal flux):

$$\mu \frac{dI_\nu}{d\tau_\nu} = I_\nu - S_\nu \quad (3)$$

128 where S_ν is the source function (either the incident solar radiation or the ther-
 129 mal blackbody emission of the atmospheric layers and the planetary surface),
 130 $d\tau_\nu$ the optical depth and $\mu = \cos(\theta)$ the cosine of the polar angle. The optical
 131 depth is defined as usual by

$$d\tau = -(\kappa_\nu + s_\nu)dz \quad (4)$$

132 where κ_ν and s_ν represent the absorption coefficient and the scattering coef-
 133 ficient respectively. The absorption coefficient for a gas mixture is calculated
 134 from the individual absorption coefficients of the gas species i :

$$\kappa_\nu = \sum_i \kappa_{\nu,i} = \sum_i \sigma_{\text{abs},i} \cdot N_i \quad (5)$$

135 where N_i is the number density and $\sigma_{\text{abs},i}$ the molecular absorption cross section
 136 of the gas species i . When no scattering occurs (i.e., $s_\nu = 0$), eq. 4 can be
 137 written in terms of the column density W_i of the gas species i as:

$$\tau = \sum_i \sigma_{\text{abs},i} \cdot W_i \quad (6)$$

138 The absorption cross section is defined by:

$$\sigma_{\text{abs}}(\nu, p, T) = \sum_j S_j(T) \cdot g_j(\nu, T, p) \quad (7)$$

139 Here, $S_j(T)$ is the temperature-dependent line strength of a particular spec-
 140 tral line j and $g_j(\nu, T, p)$ the temperature- and pressure-dependent line shape

141 function of the same line.

142 For the scattering coefficient, an analogous equation is valid:

$$s_\nu = \sum_i s_{\nu,i} = \sum_i \sigma_{y,i}(\nu) \cdot N_i \quad (8)$$

143 Here, $\sigma_{y,i}(\nu)$ is a scattering cross section of type y . In the present model,
144 Rayleigh scattering is considered.

145 The solution of eq. (4), i.e. the calculation of optical depths, is one of the key
146 elements in radiative-convective models. This solution, of course, depends on
147 the accurate calculation of the absorption cross sections.

148 From eq. (3), the necessary fluxes for eq. (2) (i.e., the thermal and the solar
149 flux) are obtained by an angular integration of the (monochromatic) intensity:

$$F_\nu = \int_\Omega d\omega \mu I_\nu \quad (9)$$

150 and a frequency integration of the (monochromatic) flux:

$$F_{\nu_1 \rightarrow \nu_2} = \int_{\nu_1}^{\nu_2} F_\nu d\nu \quad (10)$$

151 Each one of these integrations is performed independently for the two compo-
152 nents of the total flux.

153 *2.2.1 Solar radiation*

154 The solar radiation module which calculates $F_{\text{solar}}(z)$ for eq. (2) has already
155 been used by, e.g., Pavlov et al. (2000); Segura et al. (2003) or Grenfell et al.
156 (2007a) and is based on Kasting et al. (1984b) and Kasting (1988). The module
157 considers a spectral range from 0.26 to 4.5 μm in 38 intervals. It evaluates the

158 solar incident radiation at a fixed daytime average solar zenith angle of 60° .
159 Contributions to the optical depth come from gaseous absorption by water
160 and carbon dioxide (i.e., κ_ν in eq. (4)) and from Rayleigh scattering by carbon
161 dioxide, molecular nitrogen and molecular oxygen (i.e., s_ν in eq. (4)).

162 Absorption cross sections σ_{abs} for the solar code were obtained from the HI-
163 TRAN 1992 database (Rothman et al., 1992). Rayleigh scattering cross sec-
164 tions σ_{ray} are parameterized following Vardavas and Carver (1984). The fre-
165 quency integration (see also eq. (10)) of the RTE for F_{solar} in each of the 38
166 spectral intervals is parameterized by a four-term correlated-k exponential sum
167 (e.g., Wiscombe and Evans, 1977). The following angular integration (eq. (9))
168 is performed by using a quadrature δ -2-stream approximation code based on
169 Toon et al. (1989). The resulting fluxes from each spectral interval are added
170 up to yield the total solar flux $F_{\text{solar}}(z)$ at an atmospheric level z . This flux is
171 further multiplied by a factor of 0.5 to account for diurnal variation.

172 2.2.2 Thermal molecular absorption

173 The thermal (planetary) radiation module for $F_{\text{thermal}}(z)$ in eq. (2) consid-
174 ers a spectral range from 1 to 500 μm in 25 intervals. Our new thermal
175 module is called MRAC (Modified RRTM for Application in CO_2 -dominated
176 Atmospheres) and is based on the radiation scheme RRTM (Rapid Radia-
177 tive Transfer Model). RRTM was developed by Mlawer et al. (1997) and has
178 been used by numerous other modeling studies (e.g., Segura et al., 2003, 2005;
179 Grenfell et al., 2007a,b). The need for a new radiation model comes from the
180 fact that RRTM was specifically designed for conditions of modern Earth, i.e.
181 it is not adaptable to studies of atmospheres which greatly differ from mod-
182 ern atmospheric conditions (in terms of atmospheric composition, temperature
183 structure, pressure, etc.). MRAC is easily adaptable to varying conditions, as
184 is described below.

185 MRAC uses the correlated- k approach (e.g., Goody et al., 1989; Lacis and Oinas,

186 1991; Colaprete and Toon, 2003) for the frequency integration of the RTE in
 187 the thermal range, as does RRTM. The planetary surface (bottom layer of the
 188 model atmosphere) and the atmospheric layers are taken as blackbody emit-
 189 ters, according to their respective temperatures. The thermal surface emissivity
 190 is set to unity. The absorber species considered in MRAC are water, carbon
 191 dioxide and carbon monoxide. The angular integration (eq. (9)) is performed
 192 using the diffusivity approximation (as in Mlawer et al., 1997).

193 *The correlated-k method*

194 Basically, this method transfers the frequency integration (FI) of the RTE from
 195 frequency space ν to a probability space g . For the absorption cross section
 196 σ_{abs} of eq. (7) in an interval $[\nu_1, \nu_2]$, a probabilistic density distribution $f(\sigma_{\text{abs}})$
 197 (i.e., probability of occurrence for a particular value of σ_{abs}) with the following
 198 normalization condition can be defined:

$$\int_0^{\infty} f(\sigma_{\text{abs}}) d\sigma_{\text{abs}} = 1 \quad (11)$$

199 To follow conventional nomenclature in the literature regarding k -distributions,
 200 σ_{abs} is hereafter referred to as k . The function $f(\sigma_{\text{abs}}) = f(k)$ is called the k -
 201 distribution. From the k -distribution, a cumulative k -distribution $g(k)$ can be
 202 defined by

$$g(k) = \int_0^k f(k') dk' \quad (12)$$

203 The cumulative k -distribution is a strictly monotonic function and may thus
 204 be inverted from $g(k)$ to yield $k(g)$. This mapping of the frequency informa-
 205 tion ($k(\nu)$) into a single probability variable ($k(g)$) can be done because it is
 206 irrelevant at which position of the spectral interval a particular value of the
 207 absorption cross section k occurs. Performing a variable substitution in eq.
 208 (10) then leads to the following equation:

$$F_{\nu_1 \rightarrow \nu_2} = \int_{\nu_1}^{\nu_2} F(\nu) d\nu = \int_0^1 F(g) dg \quad (13)$$

209 The goal of the cumulative- k approach is to reduce the number of radiative
 210 transfer operations drastically while keeping the accuracy of line-by-line mod-
 211 els. This can be achieved with very few numbers of points in g space (see
 212 Goody et al., 1989; West et al., 1990). The g integration in eq. (13) is per-
 213 formed in MRAC by Gaussian quadrature using 16 intervals in g space (the
 214 same as used in RRTM, Mlawer et al., 1997).

215 The extension of this exact method from homogeneous to inhomogeneous at-
 216 mospheres is called the correlated- k method (e.g., Mlawer et al., 1997). Each
 217 g interval is treated as if it were a monochromatic frequency interval, i.e. the
 218 method uses the same subset of g space for all layers throughout the atmo-
 219 sphere. This implies a full frequency correlation of a specific subset of g space
 220 for all atmospheric layers. There are conditions under which this approach is
 221 exact (Goody and Yung, 1989), but usually these do not hold. However, the
 222 numerical error of the correlated- k method is generally small (Mlawer et al.,
 223 1997).

224 *Creating the new radiation scheme*

225 MRAC was originally designed to simulate atmospheres of a wide range of pos-
 226 sible terrestrial planets other than modern Earth, as stated above. Therefore, a
 227 new temperature-pressure (T - p) grid to incorporate the aforementioned (T , p)-
 228 dependence of the absorption cross sections (see eq. 7) has been introduced.
 229 In RRTM, k values are tabulated for every spectral band and every point in g
 230 space for 59 pressure levels and the associated Mid-Latitude-Summer (MLS)
 231 standard Earth temperature values as well as temperature values $T_{\text{MLS}} \pm 15$ K
 232 and $T_{\text{MLS}} \pm 30$ K, as described in Mlawer et al. (1997). The T - p grid of RRTM
 233 is thus more or less fixed to modern Earth conditions. For MRAC, we used
 234 8 pressure levels, ranging equidistantly in $\log p$ from 10^{-5} to 100 bar and 9

235 temperature points, 6 in 50 K steps from 150 K to 400 K and three additional
236 points for 500, 600, 700 K respectively. Tests showed that this grid allows for
237 an interpolation accuracy of usually better than 2-3%. Furthermore, the num-
238 ber of T - p points is consistent with previous modeling studies (Kasting et al.,
239 1993; Colaprete and Toon, 2003).

240 Figure 1 shows the range of the tabulated k -values for both RRTM and MRAC,
241 i.e. the interpolation regime of the two radiative schemes. It demonstrates that
242 RRTM can only be applied to a much narrower range of atmospheric conditions
243 in comparison to MRAC.

244 The necessary re-calculation of the k -distributions for each of the gases in-
245 cluded in MRAC (water, carbon dioxide, carbon monoxide) proceeded in three
246 steps:

247 First, the absorption cross sections for every species were calculated for each
248 T - p grid point in each of the spectral intervals where the respective species is ac-
249 tive. The line shape cut-off was set to 10 cm^{-1} from the frequency ν , i.e. the sum
250 over j in eq. (7) contains contributions from all lines within $\pm 10 \text{ cm}^{-1}$. For the
251 line shape $g_j(\nu, T, p)$, a Voigt profile was assumed. The required line parameters
252 were taken from the HiTemp 1995 database (Rothman et al., 1995). The for-
253 eign broadening parameters in HiTemp are given for air, i.e. an oxygen-nitrogen
254 mixture as a background atmosphere. However, as reported by several authors
255 (e.g., Brown et al., 2005; Toth, 2000), the foreign broadening parameters vary
256 by significant amounts when different broadening gases are considered. Thus,
257 for each type of background atmosphere, a new set of k -distributions must be
258 generated (e.g., low-oxygen atmospheres, CO_2 -dominated atmospheres, inter-
259 mediate N_2 - O_2 -atmospheres). These line parameters were then used as input
260 to a line-by-line radiative transfer model called Mirart (Schreier and Böttger,
261 2003). Mirart produced the actual absorption cross sections with a spectral
262 resolution of 10^6 equidistant points per spectral interval.

263 Second, the k -distributions $f(k)$ were calculated from the absorption cross

264 sections. From the k distribution $f(k)$, the cumulative k -distribution $g(k)$ was
265 then obtained.

266 Third, representative k values were calculated for each of the g subintervals. In
267 this step, our algorithm followed the approach of Mlawer et al. (1997), i.e. for
268 each of the 16 Gaussian subintervals in g space, an arithmetic mean absorption
269 cross section was calculated.

270 MRAC also implements a so-called binary species parameter η for transmit-
271 tance calculations. This is employed in intervals having two important absorber
272 species (for more details, see Mlawer et al., 1997 or Colaprete and Toon, 2003):

$$\eta = \frac{C_1}{C_1 + r \cdot C_2} \quad (14)$$

273 Here, $C_{1,2}$ are the concentrations of the two gases (in the case of MRAC, wa-
274 ter and carbon dioxide) and r is some specified reference ratio (mean modern
275 Earth tropospheric values). Carbon monoxide, although present in the model
276 in six spectral intervals, is not considered to be part of the binary species
277 parameter. This is partly due to the expected low concentrations in the sim-
278 ulated atmospheres (typical theoretical and measured values for early Earth
279 and Mars are below 10^{-4} volume mixing ratio), partly due to the expected low
280 temperatures (below 300 K), which means that the strong CO fundamentals
281 around $4 \mu\text{m}$ are completely outside the relevant Planck emission windows.
282 Consequently, carbon monoxide has only a reduced impact on the radiation
283 budget, compared to water and carbon dioxide. k -distributions are calculated
284 in MRAC for 5 different values of η , ranging equidistantly from 0 (CO₂ only)
285 to 1 (H₂O only).

286 Another improvement in MRAC, compared to RRTM, is the treatment of the
287 Planck function in each band. The fraction of thermal radiance associated with
288 a subset in g space is calculated from eq. (11) in Mlawer et al. (1997):

$$f_g = \frac{B_g w_g}{\overline{B}_g} \quad (15)$$

289 Here, B_g is the average Planck function of the frequencies in the subset of g
 290 space, w_g the Gaussian weight of the g interval and \overline{B}_g the average Planck
 291 function of the whole spectral band (i.e., the whole g space). As temperature,
 292 pressure and species concentrations vary, the different g subsets will correspond
 293 to different frequencies, and as such the value of B_g , thus f_g , will vary. This
 294 has been taken into account while constructing the k -distributions.

295 Mlawer et al. (1997) tabulated values of f_g for every value of the binary species
 296 parameter and for two atmospheric reference levels, one each in the troposphere
 297 and the stratosphere. In MRAC, values of f_g were tabulated for three temper-
 298 atures and two pressure levels as well as for the values of the binary species
 299 parameter. The most important factor for f_g is the binary species parameter η ,
 300 whereas the variation with temperature and pressure is rather small, although
 301 not negligible. Therefore these 6 T - p points are regarded as to be sufficient.

302 A further difference between RRTM and MRAC is the distinction between
 303 troposphere and stratosphere. In the troposphere, RRTM changes major and
 304 minor absorbers in some of the spectral intervals (see table 1 in Mlawer et al.,
 305 1997). In some spectral bands, no absorption is considered in the stratosphere,
 306 in others, the number of key species is reduced. This is done because on Earth,
 307 the chemical and physical regimes are quite different in the troposphere com-
 308 pared to those in the stratosphere. However, as this is mostly due to Earth-
 309 specific conditions (e.g., the cold trap, tropopause and temperature inversion
 310 all approximately occur at the same altitude), this distinction was not incor-
 311 porated into MRAC.

312 *2.2.3 Thermal continuum absorption*

313 Based on approximation formulations used by Kasting et al. (1984b), Kasting et al.
 314 (1984a) and Colaprete and Toon (2003), additional CO₂ and H₂O continuum
 315 absorption in the thermal region is considered. In contrast, the RRTM scheme
 316 only considers water continuum absorption (Mlawer et al., 1997).

317 Equation (16) shows the approximation for the optical depth $\tau_{\text{cont,CO}_2}$ due
 318 to CO₂ continuum absorption. The corresponding parameters are taken from
 319 Kasting et al. (1984b).

$$\tau_{\text{cont,CO}_2} = C_i W \cdot p_E \left(\frac{T_0}{T} \right)^{t_i} \quad (16)$$

320 In this equation, C_i a frequency-dependent adjustment to the path length,
 321 W the column amount of CO₂, $p_E = (1 + 0.3 \cdot C_{\text{CO}_2}) \cdot p$ (p layer pressure,
 322 C_{CO_2} concentration) an effective CO₂ broadening pressure and $T_0=300$ K is a
 323 reference temperature.

324 The optical depth $\tau_{\text{cont,H}_2\text{O}}$ due to water continuum absorption in the window
 325 region (8-12 μm) is calculated from the equation (Kasting et al., 1984a)

$$\tau_{\text{cont,H}_2\text{O}} = h_n \cdot p \cdot \frac{W_w^2}{W_t} \quad (17)$$

326 where $h_n = h_t \cdot h_\nu$ incorporates the frequency and temperature dependence, p is
 327 the pressure, W_t the total and W_w the water column of the layer. h_ν is evaluated
 328 at the high frequency interval boundary, as in Kasting et al. (1984a). We use
 329 the following approximations for h_t and h_ν , based on Kasting et al. (1984a)
 330 and Colaprete and Toon (2003):

$$h_t = e^{1800 \cdot \left(\frac{1}{T} - \frac{1}{296} \right)} \quad (18)$$

$$h_\nu = 1.25 \cdot 10^{-22} + 1.67 \cdot 10^{-19} \cdot e^{-2.62 \cdot 10^{-13} \cdot \nu} \quad (19)$$

331 Both the water and the carbon dioxide continuum absorption are considered to
 332 be approximately monochromatic over a specific spectral interval, hence their
 333 contribution to the overall absorption coefficient (see eq. (4)) is added as a
 334 constant term.

335 2.2.4 Convective adjustment

336 Convective adjustment to the lapse rate is performed whenever the calculated
 337 radiative lapse rate $\nabla_{\text{rad}}T$ exceeds the adiabatic value $\nabla_{\text{ad}}T$ (Schwarzschild
 338 criterion):

$$\nabla_{\text{rad}}T > \nabla_{\text{ad}}T \quad (20)$$

339 The adiabatic lapse rate is calculated as a standard dry adiabat in the strato-
 340 sphere. In the troposphere, a wet H₂O adiabatic lapse rate is assumed. Below
 341 273 K, the Clausius-Clapeyron-equation $\frac{d \ln(p_v)}{d \ln(T)} = \frac{m \cdot L}{R \cdot T}$ (R universal gas con-
 342 stant, m mass, L latent heat release per mass) for the saturation vapor pressure
 343 curve p_v is applied. Between 273 and 647 K, a formulation by Ingersoll (1969)
 344 is taken.

345 2.3 Atmospheric water profile

346 In every time step, the water vapor profile is re-calculated according to the
 347 new temperature profile.

348 In the troposphere, water vapor concentrations $C_{\text{H}_2\text{O}}$ are calculated from a
 349 fixed relative humidity distribution RH :

$$C_{\text{H}_2\text{O}}(T, z) = \frac{p_{\text{sat}}(T(z))}{p(z)} \cdot RH(z) \quad (21)$$

350 where p_{sat} is the saturation vapor pressure of water at the given temperature T
 351 and p the atmospheric pressure at level z . The default relative humidity profile
 352 RH follows the approach of Manabe and Wetherald (1967), with a relative
 353 humidity R_s of 80% at the surface.

$$RH(z) = R_s \cdot \frac{\frac{p(z)}{p_{\text{surface}}} - 0.02}{0.98} \quad (22)$$

354 Above the cold trap, water vapor is treated as a non-condensable gas, and its
 355 concentration is fixed at the cold trap value.

356 *2.4 Boundary conditions, initial values and parameters*

357 Since eq. (1) is a first order differential equation for the temperature, a start-
 358 ing temperature profile must be provided. In addition, a boundary condition
 359 for the radiative flux must be specified. To obtain unique equilibrium solu-
 360 tions, parameters must also be provided for the model. These include pressure
 361 parameters for the planetary top-of-atmosphere (TOA) pressure p_0 , gas con-
 362 centrations, surface albedo or solar zenith angle, for example.

363 Table 2 summarizes the boundary conditions, initial values and parameters.

364 **3 Validation of the new radiation scheme**

365 *3.1 General remarks*

366 MRAC has been tested in two different ways.

367 • Case 1: *k*-distributions

368 The calculated *k*-distributions, i.e. the model input data, have been val-
369 idated against published values to show that the algorithm creating the
370 *k*-distributions works correctly.

371 • Case 2: Earth atmosphere temperature profiles

372 Temperature profiles of an Earth-like test atmospheres (composition: N₂
373 0.77, O₂ 0.21, Ar 0.01, CO₂ $3.55 \cdot 10^{-4}$) calculated with MRAC and RRTM
374 have been compared. This was done since RRTM has been extensively
375 validated both against line-by-line codes and atmospheric measurements
376 (Mlawer et al., 1997) under modern Earth conditions.

377 Our test atmosphere has a composition close to the present day atmo-
378 sphere. However, it lacks radiative trace gases such as nitrous oxide, ozone
379 and methane, as these gases cannot be handled by MRAC yet (see above).
380 Note that due to the lack of ozone in our test atmosphere, we do not expect
381 a large stratospheric temperature maximum as is observed in the present
382 Earth atmosphere because this maximum is almost entirely due to the ab-
383 sorption of solar radiation by ozone.

384 We additionally performed test runs on a second test atmosphere (not
385 shown) which differs from the first one by its CO₂ content (100-fold increase).
386 This 100-fold increase in CO₂ represents the current limit for the RRTM
387 scheme (Segura et al., 2003, Eli Mlawer, priv. comm.).

388 These two validation approaches are discussed below.

389 *3.2 k-distributions*

390 Figures 2 and 3 compare our calculated *k*-distributions (dotted lines) with
391 previously published values (plain lines) for different water and carbon dioxide
392 bands. Published values were taken from Lacis and Oinas (1991) (H₂O, Fig.
393 2) and Mlawer et al. (1997) (CO₂, Fig. 3). Figures 2 and 3 indicate quite good
394 agreement with the published values.

395 *3.3 Earth temperature profiles*

396 The calculated temperature profiles for the test atmosphere are shown in Fig.
397 4.

398 Figure 4 implies some differences in the middle to upper stratosphere (2-6 K)
399 and small deviations ($\ll 1K$) below about 20 km. For the test atmosphere
400 with a 100-fold increase in CO₂ (not shown), the stratospheric differences are
401 even larger (up to 10 K). We interpret these differences in the temperature
402 profiles as follows:

403 Firstly, as stated above in section 2.2.2, MRAC does not differentiate between
404 troposphere and stratosphere, as is the case for RRTM. That means, spectral
405 bands where H₂O or CO₂ absorb only weak are not considered for optical depth
406 calculations in the stratosphere by RRTM (e.g., bands 6, 12-13 and 15-16). In
407 contrast, MRAC incorporates the contribution of CO₂ and H₂O to the optical
408 depth in these spectral bands. However, this contribution is usually rather
409 small.

410 Secondly, and more importantly, the differences between the stratospheric tem-
411 perature profiles occur where RRTM has to use a temperature extrapolation
412 for the absorption cross sections beyond the limits of its tabulated values.

413 Fig. 5, shows the temperature profile for our test atmosphere Earth 1. Also
414 shown is the validity range of RRTM as already indicated in Fig. 1. This rep-
415 resents the lower temperature limit for the tabulated absorption cross sections
416 in RRTM, as stated above.

417 As can be seen from Fig. 5, the calculated temperature values for the first test
418 atmosphere are below the lower RRTM validity limit. Therefore, RRTM uses
419 linear extrapolation to calculate the absorption cross sections. This introduces
420 a large extrapolation error. On average, the calculated absorption cross sec-
421 tions are a factor of 2-5 too low, depending on the spectral band. Sometimes,

422 the extrapolation performed by RRTM even yields negative absorption cross
423 sections. The interpolation errors in MRAC, on the contrary, reach only 1-2%
424 on average.

425 Figure 6 shows the radiative fluxes and heating and cooling rates calculated by
426 RRTM and MRAC in the test atmosphere Earth 1. Solar fluxes and heating
427 rates differ by much less than 1 %. The thermal down-welling fluxes calcu-
428 lated by RRTM and MRAC show large differences in the stratosphere below
429 pressures of around 10^{-2} - 10^{-3} bar, reaching up to a factor of 5 in the upper
430 stratosphere where pressures are below 10^{-4} bar. However, these differences
431 are well below 1 W m^{-2} , so are not discernible on the scale in Figure 6. The
432 up-welling fluxes differ by only about 10 % in the stratosphere, since they
433 are dominated by the tropospheric component. Hence, the calculated resulting
434 cooling rates differ only by small amounts of 0.1 - 0.4 K day^{-1} and usually lie
435 within 5-10 %, especially in the upper stratosphere.

436 In order to assess the sensitivity of the model to errors in the absorption cross
437 sections (hence, in optical depth and thermal fluxes), we artificially increased
438 the optical depth in RRTM in the most important stratospheric band, the CO_2
439 $15\mu\text{m}$ fundamental by factors of 2, 5, 10 and 20, respectively. Fig. 7 quantifies
440 the effect of these sensitivity runs on the temperature profile. Fig. 7 a) shows
441 the total optical depth calculated by RRTM and MRAC in the validation
442 runs. Clearly, in the stratosphere, RRTM under-estimates the optical depth,
443 as already discussed above.

444 Fig. 7 b) shows the temperature profiles for the two Earth validation runs with
445 MRAC and RRTM, as well as for a run with RRTM, but increased optical
446 depth by a factor of 2. This factor of 2 is representative of the error in the
447 absorption cross section calculations in the $15 \mu\text{m}$ band due to the required
448 extrapolation in the T - p -range, as shown in Figure 1. It can be seen that
449 by increasing the optical depth in RRTM artificially, the temperature profile
450 nearly reproduces the MRAC temperature profile.

451 These results show that conditions which differ too much from the Earth's
452 standard atmosphere seem to pose problems for RRTM. This limitation was
453 already noted in some of the previous studies performed with RRTM. Clearly,
454 due to the use of an expanded temperature range, MRAC performs better than
455 RRTM in these atmospheres.

456 **4 About the runs**

457 *4.1 Absorption cross sections*

458 The absorption cross sections used in the runs performed for this work (sum-
459 marized in Tables 3 and 4) were calculated assuming a N₂-CO₂-background
460 atmosphere, consisting of 95% molecular nitrogen and 5% carbon dioxide. Ac-
461 cording to Kasting and Ackerman (1986) and Toth (2000), the foreign broad-
462 ening coefficient for water is enhanced by a factor of 2 with respect to air for
463 CO₂ as a broadening gas and by a factor of 1.2 for N₂ as a broadening gas.
464 Similarly, for carbon dioxide the foreign broadening coefficient was enhanced
465 by a factor of 1.3 when N₂ was the broadening gas (Kasting and Ackerman,
466 1986). Accounting for the appropriate mixing ratios then yields an effective
467 enhancement factor by which the foreign broadening parameter from HiTemp
468 was multiplied before use in the cross section calculations described above.

469 We compared the calculated cross sections of the assumed N₂-CO₂-atmosphere
470 (95% nitrogen and 5% carbon dioxide) with cross sections for some major spec-
471 tral bands corresponding to different background atmospheres, i.e. different
472 CO₂ concentrations. These cross sections were obtained with the line-by-line
473 radiative transfer model Mirart (Schreier and Böttger, 2003). The cross sec-
474 tions from the 95%-N₂-5%-CO₂-atmosphere agree within 5 % for most of the
475 cases studied in this work, although for the runs with the lowest CO₂ concen-
476 trations, the agreement decreased to about 10 %.

478 *4.2 Model runs*

479 There were a total number of 12 nominal runs performed as shown in Table 3.

480 We assumed a constant background pressure of 0.77 bar N₂ with variable
481 amounts of CO₂. Water vapour contents of the atmosphere were calculated as
482 described in section 2.3. No other gases were present in the atmosphere, as in
483 Kasting (1987). For several values of the solar constant ($S=0.7, 0.75, 0.8, 0.85,$
484 0.9 and 0.95 present-day value), we increased the CO₂ partial pressure until
485 converged surface temperatures reached 273 K (runs 1-6) and 288 K (runs 7-
486 12), respectively. This procedure is similar to what was done by Kasting (1987).
487 The solar constant values were chosen as to loosely correspond to important
488 events throughout the Earth's history, such as the beginning of the main se-
489 quence life time of the Sun ($S=0.70$, 4.6 Gy ago), the end of the late heavy
490 bombardment ($S=0.75$, 3.8 Gy ago), the rise of oxygenesis by cyanobacteria
491 ($S=0.80$, 2.9 Gy ago), the first and the second oxidation event ($S=0.85$ and
492 $S=0.90$, 2 and 1.3 Gy ago respectively) and the Cambrian explosion ($S=0.95$,
493 0.6 Gy ago). Assigning geological ages to the solar constants used in the model
494 (see Table 3) is essential when comparing the calculated model CO₂ concentra-
495 tions to the available data and constraints on carbon dioxide. In this work, we
496 chose two approximations of the solar luminosity $S(t)$ with time. The first one
497 is from Caldeira and Kasting (1992), the second approximation is from Gough
498 (1981). The difference of these two formulations is most pronounced for earlier
499 time periods before 1-2 Gy ago, although it is rarely larger than a few percent.

500 The total surface pressure is always calculated from the relation $p_{\text{surf}} = p_{\text{CO}_2} +$
501 $p_{\text{N}_2} + p_{\text{H}_2\text{O}}$. Since we calculated surface temperatures of 273 K and 288 K,
502 the amount of surface pressure which arose from the evaporation of water is
503 about 6 mb and 17 mb, respectively. Note that the total surface pressure in

504 our model runs decreases with time, as we assume less CO₂ partial pressure
505 in our model atmospheres. There is no geological data available on the total
506 surface pressure throughout time, however, our approach of constant N₂ partial
507 pressure is consistent with assumptions made in previous studies (e.g., Kasting,
508 1987).

509 *4.3 Parameter variations of surface albedo and relative humidity profile*

510 Previous works regarding the "faint young Sun problem" have concentrated
511 on the increased greenhouse effect, as stated above in the Introduction. We
512 also studied two important parameters affecting the surface temperature in our
513 model, namely the surface albedo and the relative humidity (RH) distribution.

514 The importance of cloud coverage for the surface temperature, e.g. on early
515 Mars, has been studied by Mischna et al. (2000). The effect in their model was
516 quite large, yielding surface temperatures from 220 K to 290 K, depending
517 on cloud optical depth and cloud location. In our model, the surface albedo
518 simulates the presence of clouds, as stated above in the description of our
519 model.

520 Water vapour is a very effective greenhouse gas. In contrast to CO₂, its content
521 in the troposphere (where 99 % of the column resides) is controlled by the
522 hydrological cycle (ocean reservoir, evaporation, subsequent condensation and
523 precipitation) which is very sensitive to temperature. A critical parameter in
524 climate models is the relative humidity parametrization, which clearly has a
525 potentially large impact on the water content in the atmosphere and hence on
526 the resulting greenhouse effect.

527 In addition to the model runs described above, we therefore performed runs
528 varying surface albedo and relative humidity profiles. These runs are based on
529 runs 3 and 4 of Table 3, i.e. solar constants of $S=0.8$ and $S=0.85$. Table 4
530 summarizes the parameter variations.

531 In the runs from Table 3, the surface albedo is normally set to $A=0.21$ (see
 532 Table 2). Now, we assume surface albedos of $A \pm 10\%$, i.e. 0.19 and 0.23,
 533 respectively.

534 The relative humidity profile used for the calculation of water vapour con-
 535 centrations in Table 3 follows the approach of Manabe and Wetherald (1967)
 536 (referred to as RH=MW, see section 2.3). Here, for the additional parameter
 537 studies, we used three different RH profiles. The first one assumed a saturated
 538 troposphere (RH=1). The second profile used RH=0, i.e. water was removed
 539 from the atmosphere. These two profiles represent the lower and upper lim-
 540 its of the atmospheric water content. The third RH profile is a more realis-
 541 tic RH profile. It is based on a temperature correction to the RH profile of
 542 Manabe and Wetherald (1967) which was first proposed by Cess (1976) and
 543 later used by Vardavas and Carver (1985):

$$R = R_{\text{surface}} \cdot R_{\text{mw}}^{1-0.03(T_s-288)} \quad (23)$$

544 where $R_{\text{surface}} \cdot R_{\text{mw}}$ is the relative humidity distribution from eq. 22. This
 545 profile is referred to as RH=C. Figure 8 shows the difference between the
 546 two RH profiles from Manabe and Wetherald (1967) and Vardavas and Carver
 547 (1985). The total amount of water vapour is reduced by about 20 % by us-
 548 ing the temperature correction of Vardavas and Carver (1985) compared to
 549 Manabe and Wetherald (1967).

550 5 Results and Discussion

551 5.1 Examples of thermal structure and water profiles

552 Figure 9 shows the temperature profiles for run 3 (plain line) and run 4 (dotted
 553 line). Run 3 ($S = 0.80$) considered 20 mb CO_2 partial pressure, run 4 ($S =$

554 0.85) roughly 3 mb (see Table 3). These two runs were chosen because they
555 represent interesting points in time, such as the advent of cyanobacteria (run
556 3) and the first oxidation event (run 4).

557 Clearly, in the troposphere the temperature differences for the two runs are
558 rather small. In the lower to middle stratosphere (from around 10 to 25 km),
559 run 4 (dashed line) shows lower temperatures than run 3 (plain line). In this
560 region, absorption of solar radiation by CO₂ is the dominant heating process,
561 eventually causing a temperature inversion from the middle stratosphere up-
562 wards (seen for both runs in Fig. 9 for higher altitudes above 25-30 km). In
563 the upper stratosphere (above 25-30 km), where CO₂ radiative cooling via the
564 15 μ m fundamental band sets in, run 3 shows lower temperatures than run 4.
565 This reflects the lower flux and higher CO₂ concentrations in run 3 compared
566 to run 4.

567 However, as already noted by Segura et al. (2003), the actual strength of the
568 temperature inversion is not well determined due to less accurate transmittance
569 calculations in the solar code and may well turn out to be a mere numerical
570 problem rather than reflecting physical processes.

571 Also indicated in Fig. 9 are the convective zones for both runs. The convective
572 zone for the $S = 0.8$ case only reaches up to about 3 km altitude, whereas
573 in the $S = 0.85$ case, it extends already to about 7.5 km, which is closer to
574 the present-day, latitude-dependent value of 10-20 km. However, the lapse rate
575 remains close to the adiabatic value for several kilometres after entering the
576 regime of radiative equilibrium (above the dot-dashed lines in Fig. 9).

577 Figure 10 is similar to Fig. 9, but it shows the resulting water profiles. There
578 is considerably less water in the stratosphere for the $S = 0.85$ case due
579 to enhanced condensation. The cold trap position is indicated, as well as
580 the tropopause position, i.e. the boundary between the convective and non-
581 convective regime.

582 Figures 9 and 10 illustrate some interesting features regarding the thermal
583 structure of the atmosphere. The cold trap, i.e. the highest point up to which
584 water is allowed to condense out in the model, is no longer located near the
585 tropopause, as is the case in the atmosphere of modern Earth. It is still as-
586 sociated with a temperature inversion, but as this inversion occurs at higher
587 altitudes, cold trap and tropopause (i.e., the boundary between convective and
588 non-convective layers) are located at noticeably different altitudes. It seems
589 that the observation that tropopause, cold trap and temperature inversion oc-
590 cur at approximately the same height in the modern Earth's atmosphere is
591 somewhat coincidental.

592 *5.2 Climatic constraints on CO₂ partial pressures*

593 The results of the 12 nominal runs (see Table 4) are summarized in Fig. 11. The
594 lower plain line indicates the CO₂ partial pressures corresponding to calculated
595 surface temperatures of 273 K (runs 1-6), the upper plain line shows the partial
596 pressures for surface temperatures of 288 K (runs 7-12). For comparison, the
597 dashed line shows the partial pressures as calculated by Kasting (1987). Fig. 11
598 shows that our new radiative scheme requires considerably less CO₂ (about a
599 factor of 2-15) to achieve an ice-free surface than the study of Kasting (1987).

600 Note that the radiative transfer scheme used by Kasting (1987) was applicable
601 to this type of atmospheres, as is the one we used.

602 Also indicated in Fig. 11 are the upper limits of CO₂ partial pressures as
603 inferred from sedimentary data.

604 Several attempts have been made to constrain the CO₂ content of the early
605 Earth atmosphere. For example, among others, Rye et al. (1995), Hessler et al.
606 (2004) and Towe (1985) have placed upper limits on CO₂ partial pressures dur-
607 ing different periods of the mid-Archaean to early Proterozoic of approximately
608 10-100 PAL (Present Atmospheric Level), depending on temperature. These

609 limits were based on experimental sediment data and on biological consid-
610 erations. Rye et al. (1995) and Hessler et al. (2004) argued for upper limits
611 on CO₂ partial pressures based on the observations that in ancient Archaean
612 rocks, siderites are missing. Towe (1985) stated atmospheric upper levels of
613 CO₂ based on the observation that anaerobic photosynthesis and nitrogen fix-
614 ation (which are both believed to be evolutionary ancient) are incompatible
615 with high CO₂ concentrations.

616 Previous climate studies of the early Earth's atmosphere calculated very high
617 CO₂ partial pressures in order to raise the surface temperature above 273 K.
618 The model CO₂ values were generally above 50 mb well into Proterozoic age
619 (e.g., Kasting 1987, see also Fig. 11). However, the experimental data from
620 sediments and biology (see above) were of the order of several mb, i.e. an
621 order of magnitude lower. This contradiction is known as the "faint young Sun
622 problem".

623 Fig. 11 however shows that for the late Archaean (solar constant $S=0.85$), our
624 new results are compatible with the paleosol records, hence the "faint young
625 Sun problem" might be resolved for this time period.

626 One should note that the absence of methane, ozone, ammonia or other green-
627 house gases in our results implies that we calculated only a lower limit for
628 surface temperatures. Photochemical models of the anoxic Archaean and low-
629 oxygen Proterozoic atmospheres have shown that methane could build up to
630 concentrations of the order of 10^{-3} (Pavlov et al., 2003) which could also have
631 contributed to the greenhouse effect. Haqq-Misra et al. (2008) proposed higher
632 hydrocarbons such as C₂H₆ in a methane-rich atmosphere as radiative gases.
633 Those effects were not investigated here. Our studies imply, however, that
634 much less to none additional greenhouse gases are required to warm the early
635 Earth.

636 *5.2.1 Effect of parameter variations of surface albedo and relative humidity*

637 Table 4 summarizes the results of the parameter variations. Shown are the val-
638 ues of CO₂ partial pressure required to obtain the desired surface temperature
639 of 273 K.

640 Upon lowering the surface albedo value from 0.23 to 0.19, the partial pressure
641 of CO₂ required to keep the surface at 273 K is reduced from 28.5 mb to 11.0
642 mb (at $S=0.80$) and from 5.5 mb to 1.5 mb (at $S=0.85$). This is a lowering of
643 the amount of CO₂ by factors of 2.6 and 3.7, respectively.

644 When changing the RH profile from saturated (RH=1) to water-free condi-
645 tions (RH=0), the necessary partial pressure of CO₂ has to be increased from
646 4.9 mb to 266.8 mb ($S=0.80$) and from 0.6 mb to 180.6 mb ($S=0.85$). How-
647 ever, like expected, the comparison between the more realistic RH profiles
648 of Manabe and Wetherald (1967) and Cess (1976) yields much smaller differ-
649 ences. When changing the RH profile from RH=MW to RH=C, CO₂ partial
650 pressures must be increased from 19.1 mb to 27.3 mb ($S=0.80$) and from 2.9
651 mb to 4.9 mb ($S=0.85$). These differences amount to 43 % and 69 %, respec-
652 tively, which is much lower than the differences obtained by varying the surface
653 albedo.

654 These parameter variations demonstrated that the surface albedo, hence clouds,
655 is a very important parameter in view of the surface temperature. The results
656 obtained imply that the latter is probably more important than the RH profile,
657 although the RH profile has to be incorporated more consistently to accurately
658 constrain CO₂ partial pressures for the "faint young Sun" problem. This calls
659 for a more elaborated 1D model incorporating clouds and cloud formation as
660 was done by, e.g., Colaprete and Toon (2003) for early Mars. In the future, we
661 plan to add clouds to our code.

662 The results of the parameter variations, however, did not significantly change
663 our main conclusion, namely that the CO₂ values for the late Archaean cal-

664 culated by our improved model are consistent with observational data. The
665 CO₂ values obtained for the parameter variations range between 1.5-5.5 mb
666 of partial pressure. This is still close to the values inferred from the paleosol
667 record.

668 **6 Summary**

669 In this work, we addressed the "faint young Sun problem" of the ice-free early
670 Earth. In order to do this, we applied a one-dimensional radiative-convective
671 model to the atmosphere of the early Earth. Our model included updated
672 absorption coefficients in the thermal radiative transfer scheme.

673 The validations done for the new radiative transfer scheme have been described.
674 The new scheme is found to perform significantly better than a previous scheme
675 under conditions deviating from the modern Earth atmosphere.

676 We then studied the effect of enhanced carbon dioxide concentrations and
677 parameter variations of the surface albedo and the relative humidity profiles
678 on the surface temperature of the early Earth with the improved model.

679 Our new model simulations suggest that the amount of CO₂ needed to keep
680 the surface of the early Earth from freezing is significantly less (up to an order
681 of magnitude) than previously thought (see Figure 11).

682 For the late Archaean and early Proterozoic period (around 2-2.5 Gy ago), the
683 calculated amount of CO₂ (2.9 mb partial pressure) which is needed to obtain
684 a surface temperature of 273 K is compatible with the amount inferred from
685 geological data, contrary to previous studies (see Figure 11). The apparent
686 contradiction between model constraints on CO₂ and sediment data disappears
687 for this time period.

688 Upon varying model parameters such as the surface albedo and relative hu-

689 midity profile, we found this conclusion to be robust. The calculated CO₂
690 partial pressures for the late Archaean (1.5-5.5 mb) are still consistent with
691 the geological evidence.

692 **Acknowledgements**

693 We are grateful to Jim Kasting and Eli Mlawer for useful discussion while cre-
694 ating the new radiation scheme. Furthermore, we are grateful to Viola Vogler
695 for help in doing some of the plots in this paper.

696 We thank the two anonymous referees for their constructive remarks which
697 helped to improve and clarify this paper.

698 **References**

- 699 Brown, L. R., Benner, C., Devi, V. M., Smith, M. A. H., Toth, R. A., 2005.
700 Line mixing in self- and foreign-broadened water vapor at 6 μm . *Journal of*
701 *Molecular Structure* 742, 111122.
- 702 Caldeira, K., Kasting, J. F., Dec. 1992. The life span of the biosphere revisited.
703 *Nature* 360, 721–723.
- 704 Cess, R. D., 1976. Climatic change: An appraisal of atmospheric feedback
705 mechanisms employing zonal climatology. *J. Atmospheric Sciences* 33, 1831–
706 1843.
- 707 Colaprete, A., Toon, O. B., Apr. 2003. Carbon dioxide clouds in an early dense
708 Martian atmosphere. *Journal of Geophysical Research (Planets)* 108, 5025.
- 709 Goody, R., West, R., Chen, L., Crisp, D., Dec. 1989. The correlated-k method
710 for radiation calculations in nonhomogeneous atmospheres. *J. Quant. Spec-*
711 *troscopy and Radiative Transfer* 42, 539–550.
- 712 Goody, R. M., Yung, Y. L., 1989. *Atmospheric radiation: Theoretical basis.*
713 2nd ed., New York, NY: Oxford University Press.
- 714 Gough, D. O., Nov. 1981. Solar interior structure and luminosity variations.
715 *Solar Physics* 74, 21–34.
- 716 Grenfell, J. L., Griebmeier, J.-M., Patzer, B., Rauer, H., Segura, A., Stadel-
717 mann, A., Stracke, B., Titz, R., Von Paris, P., Feb. 2007a. Biomarker Re-
718 sponse to Galactic Cosmic Ray-Induced NO_x and the Methane Greenhouse
719 Effect in the Atmosphere of an Earth-Like Planet Orbiting an M Dwarf Star.
720 *Astrobiology* 7, 208–221.
- 721 Grenfell, J. L., Stracke, B., von Paris, P., Patzer, B., Titz, R., Segura, A.,
722 Rauer, H., Apr. 2007b. The response of atmospheric chemistry on earthlike
723 planets around F, G and K Stars to small variations in orbital distance.
724 *Planetary and Space Science* 55, 661–671.
- 725 Haqq-Misra, J., Domagal-Goldman, S., Kasting, P., Kasting, J. F., 2008. A
726 Revised, Hazy Methane Greenhouse for the Archaean Earth. accepted in
727 *Astrobiology*.

728 Hessler, A., Lowe, D., Jones, R., Bird, D., Apr. 2004. A lower limit for atmo-
729 spheric carbon dioxide levels 3.2 billion years ago. *Nature* 428, 736–738.

730 Ingersoll, A. P., Nov. 1969. The Runaway Greenhouse: A History of Water on
731 Venus. *J. Atmospheric Sciences* 26, 1191–1198.

732 Jenkins, G. S., 2000. Global climate model high-obliquity solutions to the
733 ancient climate puzzles of the Faint-Young Sun Paradox and low-latitude
734 Proterozoic Glaciation. *J. Geophys. Res.* 105, 7357–7370.

735 Kasting, J. F., Feb. 1987. Theoretical constraints on oxygen and carbon dioxide
736 concentrations in the Precambrian atmosphere. *Precambrian Research* 34,
737 205–229.

738 Kasting, J. F., Jun. 1988. Runaway and moist greenhouse atmospheres and
739 the evolution of earth and Venus. *Icarus* 74, 472–494.

740 Kasting, J. F., Ackerman, T. P., Dec. 1986. Climatic consequences of very
741 high carbon dioxide levels in the Earth’s early atmosphere. *Science* 234,
742 1383–1385.

743 Kasting, J. F., Howard, M. T., 2006. Atmospheric composition and climate on
744 the early Earth. *Phil. Trans. R. Soc. B* 361, 1733–1742.

745 Kasting, J. F., Pollack, J. B., Ackerman, T. P., Mar. 1984a. Response of earth’s
746 atmosphere to increases in solar flux and implications for loss of water from
747 Venus. *Icarus* 57, 335–355.

748 Kasting, J. F., Pollack, J. B., Crisp, D., 1984b. Effects of high CO₂ levels on
749 surface temperature and atmospheric oxidation state of the early Earth. *J.*
750 *Atmospheric Chemistry* 1, 403–428.

751 Kasting, J. F., Whitmire, D. P., Reynolds, R. T., Jan. 1993. Habitable Zones
752 around Main Sequence Stars. *Icarus* 101, 108–128.

753 Knauth, P., Lowe, D. R., 2003. High Archean climatic temperature inferred
754 from oxygen isotope geochemistry of cherts in the 3.5 Ga Swaziland Super-
755 group, South Africa. *GSA Bull.* 115, 566–580.

756 Lacis, A. A., Oinas, V., May 1991. A description of the correlated-k distribution
757 method for modelling nongray gaseous absorption, thermal emission, and
758 multiple scattering in vertically inhomogeneous atmospheres. *J. Geophys.*

759 Res. 96, 9027–9064.

760 Manabe, S., Wetherald, R. T., May 1967. Thermal Equilibrium of the At-
761 mosphere with a Given Distribution of Relative Humidity. *J. Atmospheric*
762 *Sciences* 24, 241–259.

763 Minton, D. A., Malhotra, R., May 2007. Assessing the Massive Young Sun
764 Hypothesis to Solve the Warm Young Earth Puzzle. *Astrophysical Journal*
765 660, 1700–1706.

766 Mischna, M. A., Kasting, J. F., Pavlov, A., Freedman, R., Jun. 2000. Influence
767 of carbon dioxide clouds on early martian climate. *Icarus* 145, 546–554.

768 Mlawer, E. J., Taubman, S. J., Brown, P. D., Iacono, M. J., Clough, S. A., Jul.
769 1997. Radiative transfer for inhomogeneous atmospheres: RRTM, a validated
770 correlated-k model for the longwave. *J. Geophys. Res.* 102, 16663–16682.

771 Mojzsis, S. J., Arrhenius, G., McKeegan, K. D., Harrison, T. M., Nutman,
772 A. P., Friend, C. R. L., Nov. 1996. Evidence for life on Earth before 3,800
773 million years ago. *Nature* 384, 55–59.

774 Pavlov, A. A., Brown, L. L., Kasting, J. F., Oct. 2001. UV shielding of NH₃
775 and O₂ by organic hazes in the Archean atmosphere. *J. Geophys. Res.* 106,
776 23267–23288.

777 Pavlov, A. A., Hurtgen, M. T., Kasting, J. F., Arthur, M. A., Jan. 2003.
778 Methane-rich Proterozoic atmosphere? *Geology* 31, 87–90.

779 Pavlov, A. A., Kasting, J. F., Brown, L. L., Rages, K. A., Freedman, R., May
780 2000. Greenhouse warming by CH₄ in the atmosphere of early Earth. *J.*
781 *Geophys. Res.* 105, 11981–11990.

782 Robert, F., Chaussidon, M., Oct. 2006. A palaeotemperature curve for the
783 Precambrian oceans based on silicon isotopes in cherts . *Nature* 443, 969–
784 972.

785 Rosing, M. T., Frei, R., Jan. 2004. U-rich Archaean sea-floor sediments from
786 Greenland - indications of >3700 Ma oxygenic photosynthesis. *Earth and*
787 *Planetary Science Letters* 217, 237–244.

788 Rothman, L. S., Gamache, R. R., Tipping, R. H., Rinsland, C. P., Smith,
789 M. A. H., Benner, D. C., Devi, V. M., Flaud, J.-M., Camy-Peyret, C., Perrin,

790 A., 1992. The HITRAN molecular data base - Editions of 1991 and 1992. J.
791 Quant. Spectroscopy and Radiative Transfer 48, 469–507.

792 Rothman, L. S., Wattson, R. B., Gamache, R., Schroeder, J. W., McCann,
793 A., Jun. 1995. HITRAN HAWKS and HITEMP: high-temperature molec-
794 ular database. In: Dainty, J. C. (Ed.), Proc. SPIE Vol. 2471, p. 105-111,
795 Atmospheric Propagation and Remote Sensing IV. Presented at the Society
796 of Photo-Optical Instrumentation Engineers (SPIE) Conference.

797 Rye, R., Kuo, P. H., Holland, H. D., Dec. 1995. Atmospheric carbon dioxide
798 concentrations before 2.2 billion years ago. Nature 378, 603–605.

799 Sagan, C., Chyba, C., 1997. The early faint sun paradox: Organic shielding of
800 ultraviolet-labile greenhouse gases. Science 276, 1217–1221.

801 Sagan, C., Mullen, G., Jul. 1972. Earth and Mars: Evolution of Atmospheres
802 and Surface Temperatures. Science 177, 52–56.

803 Schreier, F., Böttger, U., 2003. MIRART, a line-by-line code for infrared at-
804 mospheric radiation computations including derivatives. Atmospheric and
805 Oceanic Optics 16, 262–268.

806 Segura, A., Kasting, J. F., Meadows, V., Cohen, M., Scalo, J., Crisp, D., Butler,
807 R. A. H., Tinetti, G., Dec. 2005. Biosignatures from Earth-Like Planets
808 Around M Dwarfs. Astrobiology 5, 706–725.

809 Segura, A., Krelove, K., Kasting, J. F., Sommerlatt, D., Meadows, V., Crisp,
810 D., Cohen, M., Mlawer, E., Dec. 2003. Ozone Concentrations and Ultraviolet
811 Fluxes on Earth-Like Planets Around Other Stars. Astrobiology 3, 689–708.

812 Shaviv, N. J., Dec. 2003. Toward a solution to the early faint Sun paradox: A
813 lower cosmic ray flux from a stronger solar wind. J. Geophys. Res. (Space
814 Physics) 108, 1437.

815 Shields, G. A., Kasting, J. F., 2007. Palaeoclimatology: Evidence for hot early
816 oceans? Nature 447, E1.

817 Sleep, N. H., Hessler, A. M., Jan. 2006. Weathering of quartz as an Archean
818 climatic indicator. Earth and Planetary Science Letters 241, 594–602.

819 Toon, O. B., McKay, C. P., Ackerman, T. P., Santhanam, K., 1989. Rapid
820 calculation of radiative heating rates and photodissociation rates in inhom-

821 geneous multiple scattering atmospheres. *J. Geophys. Res.* 94, 16287–16301.

822 Toth, R., 2000. Air- and N₂-Broadening Parameters of Water Vapor: 604 to
823 2271 cm⁻¹. *J. Molec. Spectroscopy* 201, 218–243.

824 Towe, K., 1985. Habitability of the Early Earth - Clues from the Physiology
825 of Nitrogen Fixation and Photosynthesis. *Origins of Life* 15, 235–250.

826 Vardavas, I. M., Carver, J. H., Oct. 1984. Solar and terrestrial parameter-
827 izations for radiative-convective models. *Planetary and Space Science* 32,
828 1307–1325.

829 Vardavas, I. M., Carver, J. H., Oct. 1985. Atmospheric temperature response
830 to variations in CO₂ concentration and the solar-constant. *Planetary and*
831 *Space Science* 33, 1187–1207.

832 West, R., Crisp, D., Chen, L., Mar. 1990. Mapping transformations for broad-
833 band atmospheric radiation calculations. *J. Quant. Spectroscopy and Ra-*
834 *diative Transfer* 43, 191–199.

835 Wiscombe, W. J., Evans, J., 1977. Exponential-sum fitting of radiative trans-
836 mission functions. *Journal of Computational Physics* 24, 416–444.

837 **Figure captions**

838 Figure 1:

839 Range of T - p values used to obtain absorption cross sections in the two radia-
840 tive schemes RRTM (light grey) and MRAC (dark grey).

841

842 Figure 2:

843 Cumulative k distribution for parts of the $6.3 \mu\text{m}$ H_2O fundamental band,
844 $T=240 \text{ K}$ and $p=10 \text{ mb}$: Comparison between Lacis and Oinas (1991) (plain
845 line) and our algorithm (dotted).

846

847 Figure 3:

848 Cumulative k distribution for parts of the $15 \mu\text{m}$ CO_2 fundamental band
849 between 630 and 700 cm^{-1} , $T=260 \text{ K}$ and $p=507 \text{ mb}$: Comparison between
850 Mlawer et al. (1997) (plain line) and our algorithm (dotted).

851

852 Figure 4:

853 Comparison of validation temperature profiles (RRTM plain line, MRAC dot-
854 ted line).

855

856 Figure 5:

857 Limits of the RRTM temperature grid. Atmospheric conditions as for the stan-
858 dard CO_2 case in fig. 4, RRTM profile (plain), MRAC (dotted). The shaded
859 area designates the validity range of RRTM as already indicated in fig. 1.

860

861 Figure 6:

862 Flux profiles (thermal and solar up- and down-welling fluxes) (left panel) and
863 heating and cooling rates (right panel) calculated by the two radiative schemes
864 in the test atmosphere.

865

866 Figure 7:

867 Effect of variations in the optical depth on the temperature profile calculated
868 by RRTM: Left panel, total optical depth, right panel, temperature profiles.

869

870 Figure 8:

871 Differences of the two relative humidity profiles used for the parameter varia-
872 tions

873

874 Figure 9:

875 Temperature profiles for runs with solar constants of $S = 0.8$ (run 3, plain
876 line) and $S = 0.85$ (run 4, dotted); the background pressure is 0.77 bar of N_2 .
877 The convective zones are indicated for both runs.

878

879 Figure 10:

880 Water profiles for runs with solar constants of $S = 0.8$ (run 3, plain line) and
881 $S = 0.85$ (run 4, dashed); the background pressure is 0.77 bar of N_2 . Cold trap
882 positions and tropopause positions are indicated for both runs.

883

884 Figure 11:

885 Minimal values of CO_2 partial pressure required to obtain chosen surface tem-

886 peratures of 273 K and 288 K at a fixed N_2 partial pressure for different solar
887 constants: shown are the curves for the new model (plain lines, upper line
888 288 K, lower line 273 K) and the model of Kasting (1987) (dashed)). Symbols
889 are included which represent the upper CO_2 limits derived from the sediment
890 record (\square : age conversion by Caldeira and Kasting (1992), \triangle : age conversion
891 by Gough (1981)).

Table 1

Contribution of model species to the temperature profile via radiative transfer for solar or thermal radiation, adiabatic lapse rate formulations or heat capacity contributions (x: active species, -: inactive species)

Gas	Solar	Rayleigh	Thermal	Continuum	Lapse Rate	Heat Cap.
N ₂	-	x	-	-	-	x
H ₂ O	x	-	x	x	x	-
O ₂	-	x	-	-	-	x
Ar	-	-	-	-	-	x
CO ₂	x	x	x	x	-	x
CO	-	-	x	-	-	x

Table 2

Initial values, boundary conditions and parameters in the model (IV: initial value, BC: boundary condition, P: parameter)

Quantity	Value	Type
T_0 -profile	US Standard 1976	IV
TOA incident flux	solar spectrum	BC
TOA p_0	$6.6 \cdot 10^{-5}$ bar	P
Surface albedo	0.21	P
Zenith angle	60°	P

Table 3

Summary of model runs performed for this work (partial pressures p_{N_2} and p_{CO_2} and surface pressure p_{surf} are in mb, surface temperature T_{surf} in K)

Runs	solar constant S	p_{surf}	p_{CO_2}	p_{N_2}	T_{surf}
1	0.70	911	135.3	770	273
2	0.75	833	57.2	770	273
3	0.80	795	19.1	770	273
4	0.85	779	2.9	770	273
5	0.90	776	0.3	770	273
6	0.95	776	0.03	770	273
7	0.70	1192	405.6	770	288
8	0.75	1055	268.1	770	288
9	0.80	942	155.0	770	288
10	0.85	863	76.2	770	288
11	0.90	820	33.1	770	288
12	0.95	797	9.8	770	288

Table 4

Summary of sensitivity runs performed (RH profiles: MW Manabe and Wetherald (1967), C Cess (1976)). Partial CO₂ pressure p_{CO_2} to reach 273 K in mb.

Run number	solar constant S	RH profile	Surface albedo	T_{surf}	p_{CO_2}
1a	0.80	MW	0.19	273	11.0
2a	0.80	MW	0.21	273	19.1
3a	0.80	MW	0.23	273	28.5
4a	0.85	MW	0.19	273	1.5
5a	0.85	MW	0.21	273	2.9
6a	0.85	MW	0.23	273	5.5
7a	0.80	MW	0.21	273	19.1
8a	0.80	C	0.21	273	27.3
9a	0.80	1	0.21	273	4.9
10a	0.80	0	0.21	273	266.8
11a	0.85	MW	0.21	273	2.9
12a	0.85	C	0.21	273	4.9
13a	0.85	1	0.21	273	0.6
14a	0.85	0	0.21	273	180.6

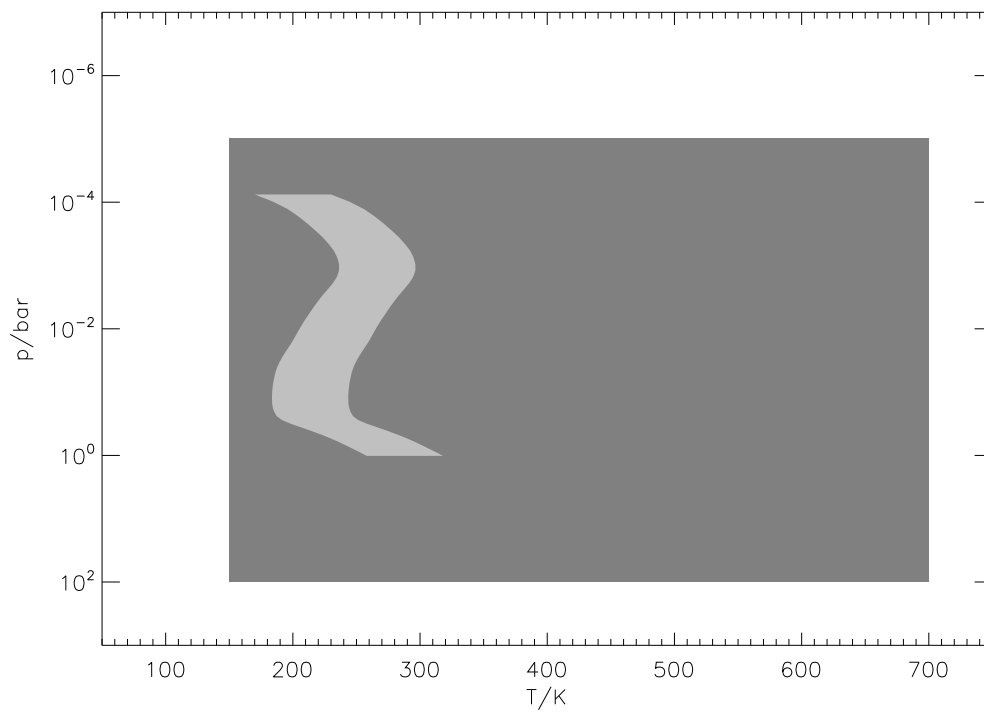


Fig. 1.

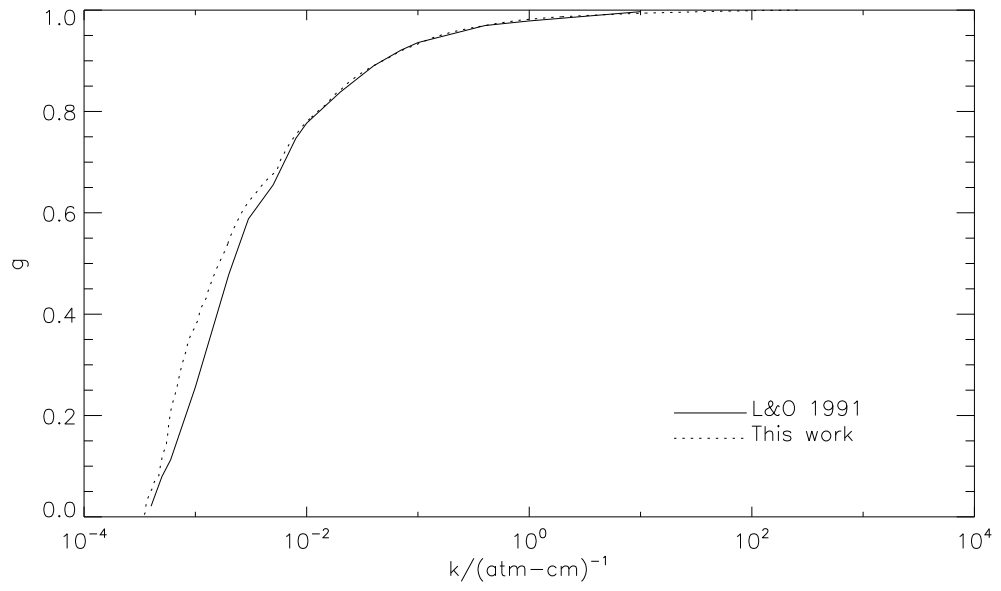


Fig. 2.

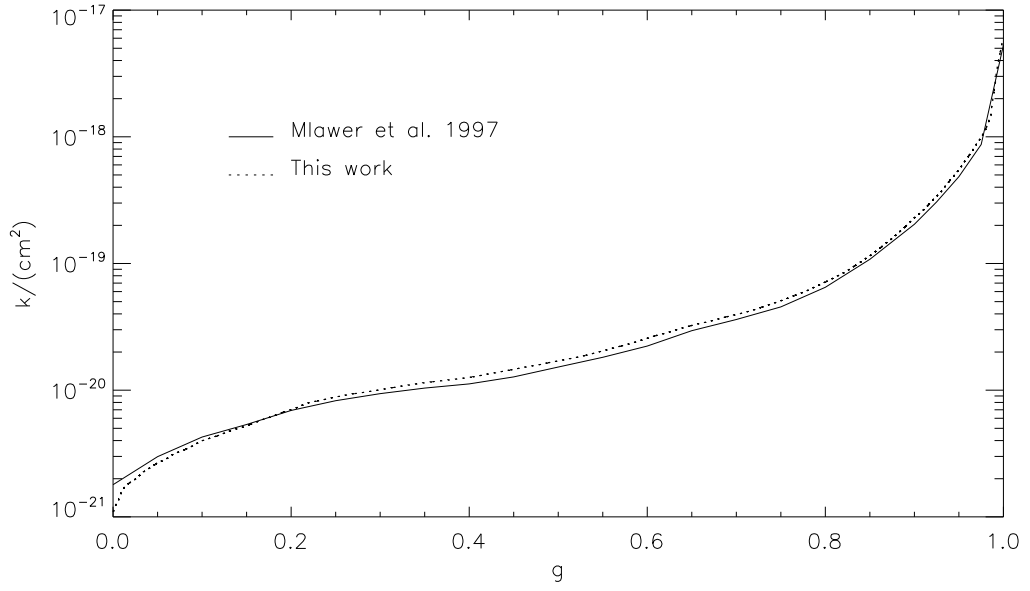


Fig. 3.

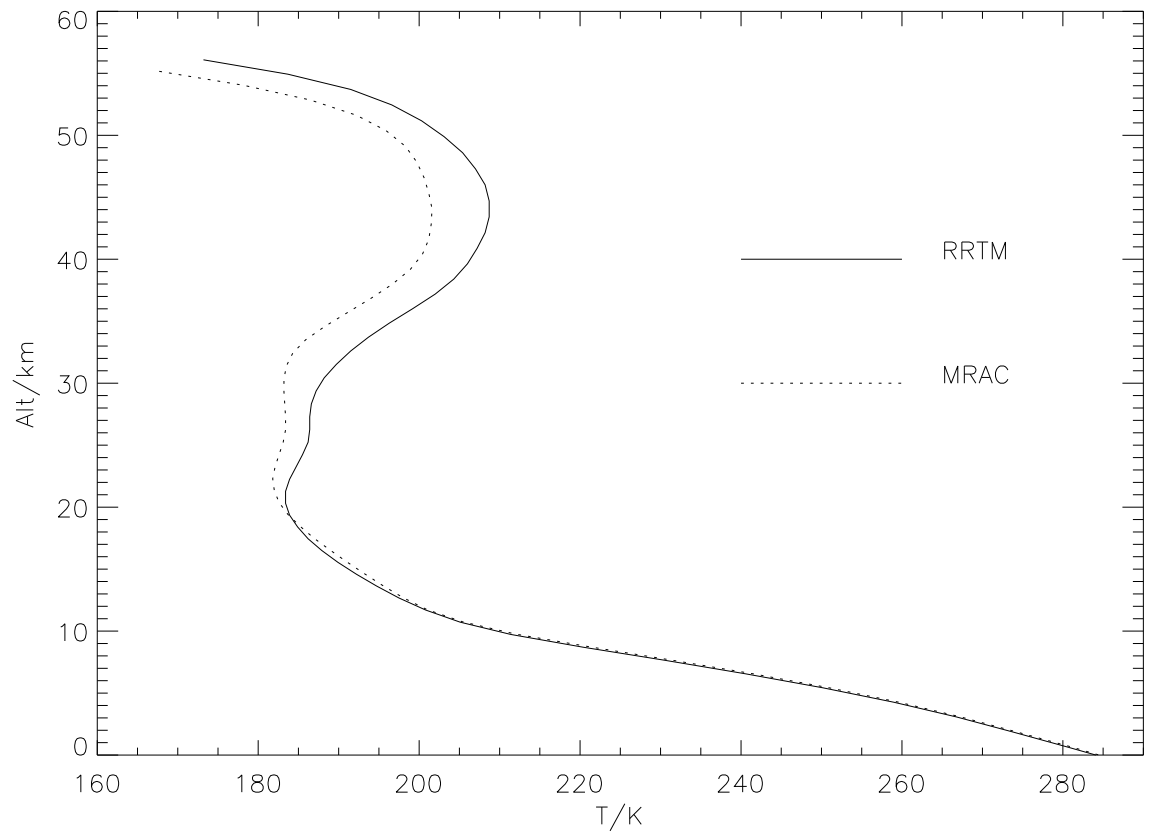


Fig. 4.

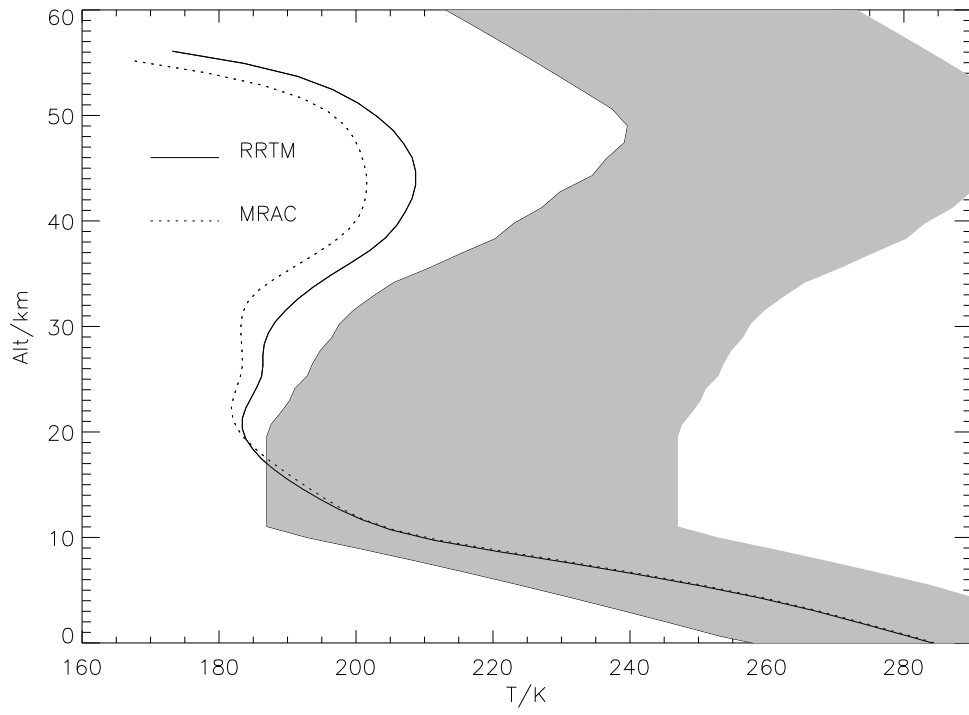


Fig. 5.

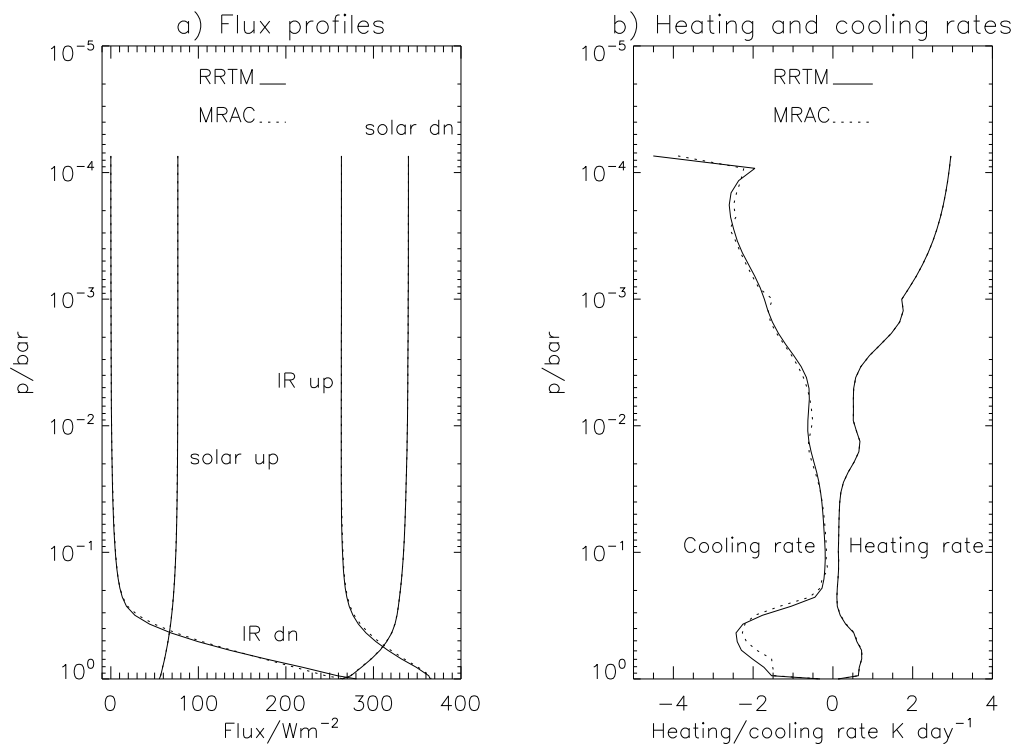


Fig. 6.

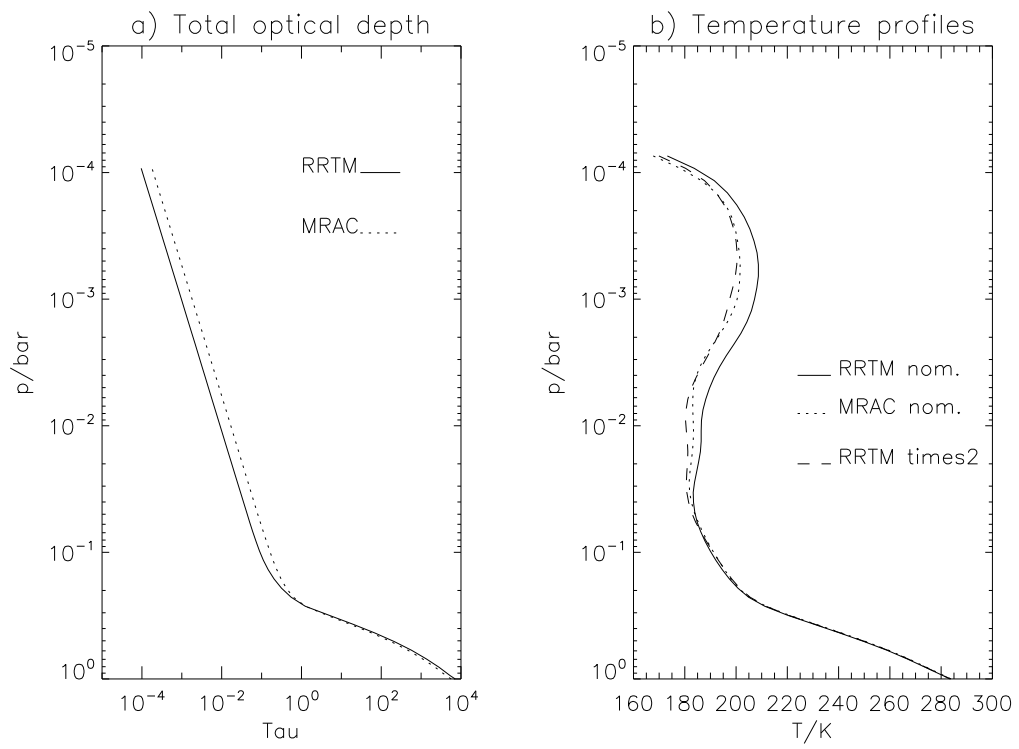


Fig. 7.

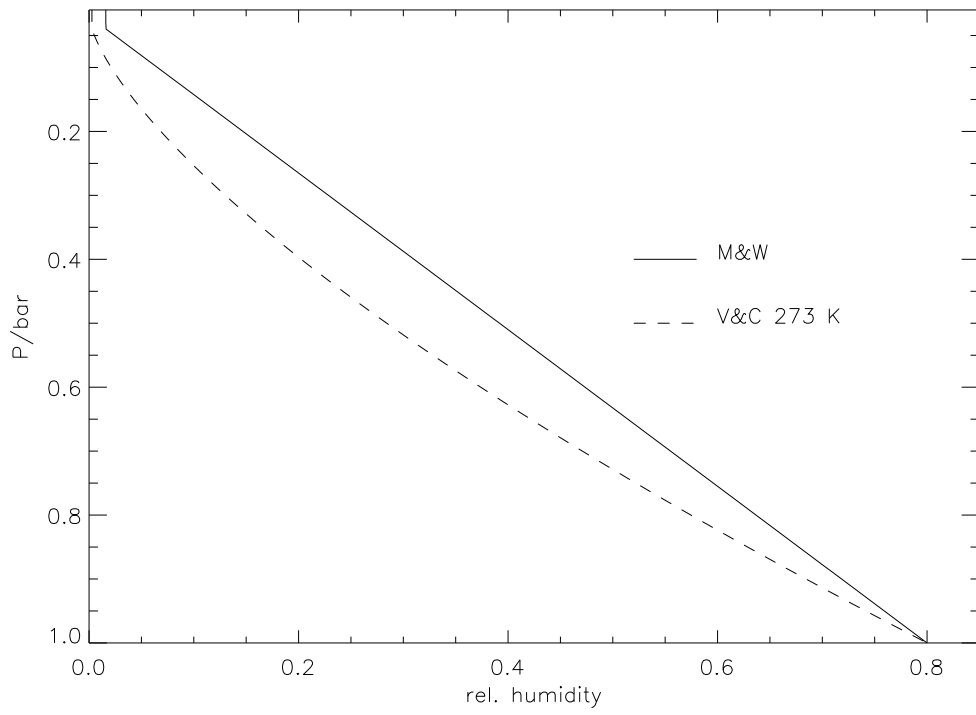


Fig. 8.

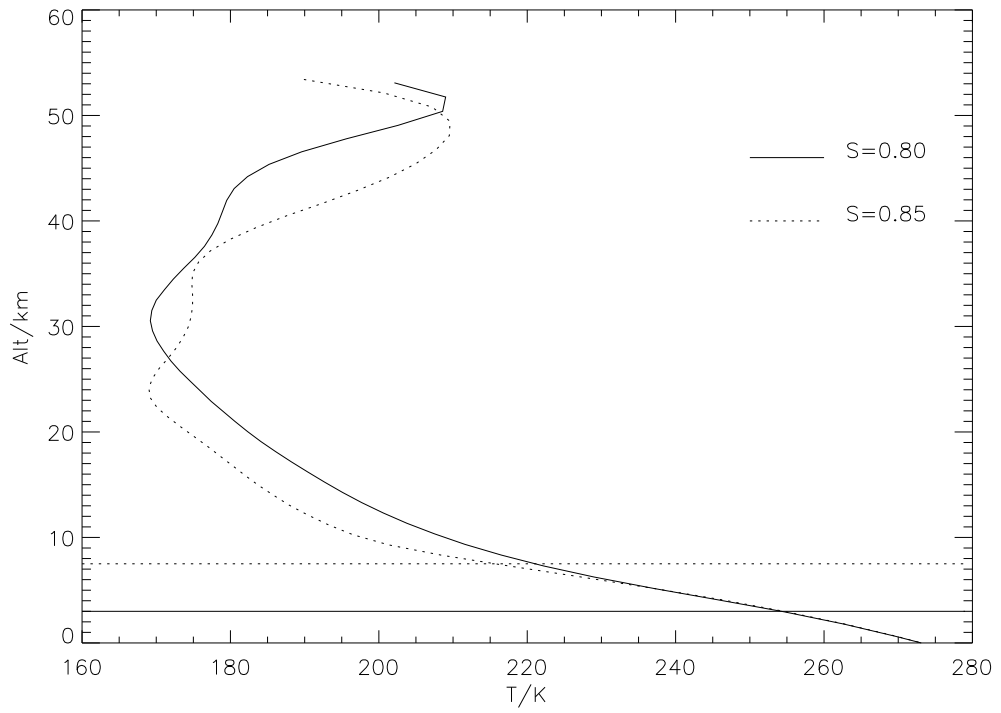


Fig. 9.

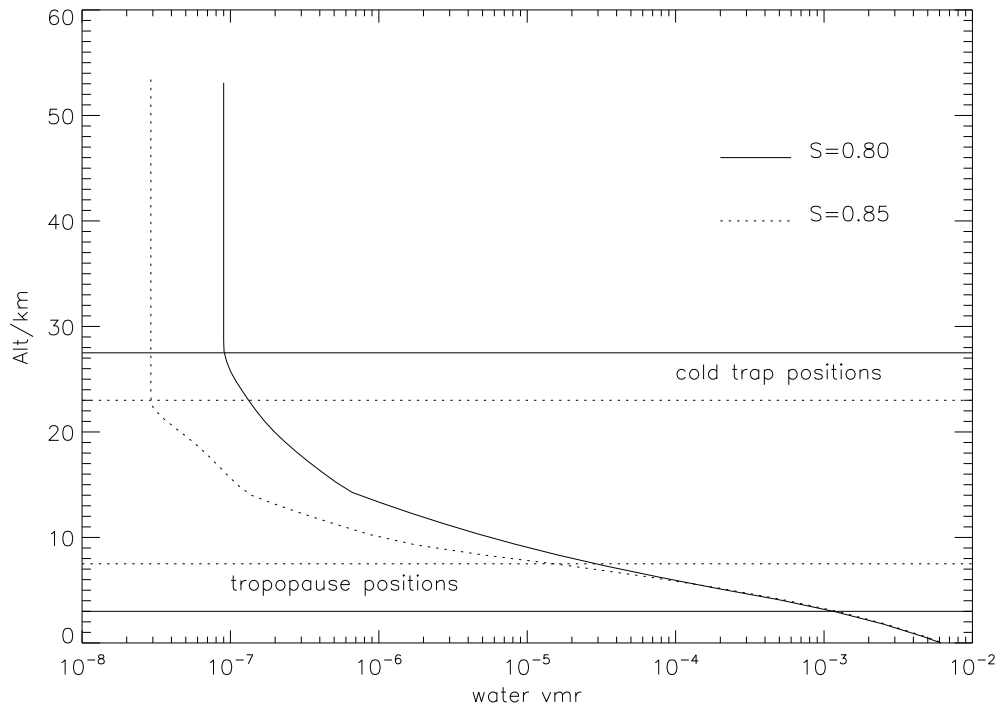


Fig. 10.

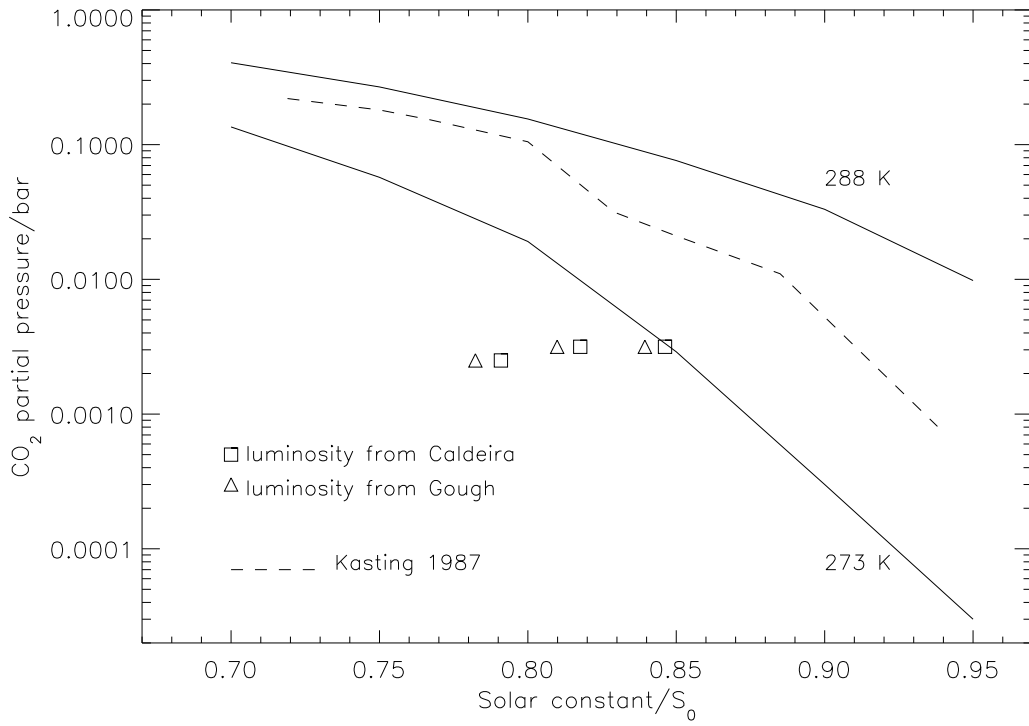


Fig. 11.